


Retrosynthetic design of core–shell nanoparticles for thermal conversion to monodisperse high-entropy alloy nanoparticles

Received: 29 April 2023

Accepted: 1 September 2023

Published online: 05 October 2023

 Check for updates

Nabojit Kar , Maximilian McCoy , Joshua Wolfe , Sandra L. A. Bueno, Ibrahim H. Shafei  & Sara E. Skrabalak  

High-entropy alloys (HEAs) consisting of five or more elements have gained considerable attention due to their distinctive properties. However, synthesizing monodisperse HEA nanoparticles (NPs) is challenging through colloidal chemistry due to differences in the reduction rates of metal precursors and poor understanding of reaction intermediates. Here we propose a general approach to HEA NPs through an NP conversion pathway, where two-phase core–shell NPs are predictably synthesized via colloidal chemistry and then converted into single-phase HEA NPs by thermal annealing. This study establishes the necessary synthesis principles for the precursor core–shell NPs by considering the relative redox potentials of metal or metal precursors and the inherent lattice properties of the selected metals. Once monodisperse core–shell NPs were synthesized, they were converted into single-phase HEA NPs (constituent metals studied include Pd, Cu, Pt, Ni, Co, Au, Ag and Sn) by a simple annealing procedure that is suitable for different NP supports. We demonstrate the ability to manipulate the degree of intermixing between the core and shell phases and the generality of this NP conversion strategy to monodisperse HEA NPs.

Alloys have a rich history, where the mixing of two or more metals can endow materials with interesting properties. Most studied alloys consisted of a primary element with small amounts of a secondary element¹. This dominance is due to the typically limited solubility of components when targeting greater compositional complexity². However, both Yeh et al. and Cantor et al. outlined that higher-order alloys may be possible by increasing the configurational entropy of mixing above the enthalpy of compound formation, introducing the study of high-entropy alloys (HEAs) where materials consisting of five or more elements ranging from 5 to 35 atomic percentage (at%) were generally assumed to have sufficiently high configurational entropy for alloy formation^{3,4}. These alloys have gained considerable attention owing to their distinctive properties such as highly distorted lattices that arise

from the mixing of atoms of different sizes and a near continuum of surface electronic states^{1,5,6}. Additionally, sluggish atomic diffusion of the atoms ensures HEAs remain stable in corrosive environments⁷. These properties make HEAs promising in mechanical and catalytic applications, particularly when prepared in nanostructured form^{8–11}.

The first discrete HEA nanoparticles (NPs) were reported by Yao et al. using a carbothermal shock method¹². The method is scalable and allows for size and compositional control of the HEA NPs. The generality of mixed metal phases can be attributed to the rapid cooling in the carbothermal shock method, which facilitates kinetic control, meaning some NP phases may be metastable. However, comprehensive understanding of the phase behaviour is impeded by the inability to characterize intermediate NPs produced by this method.

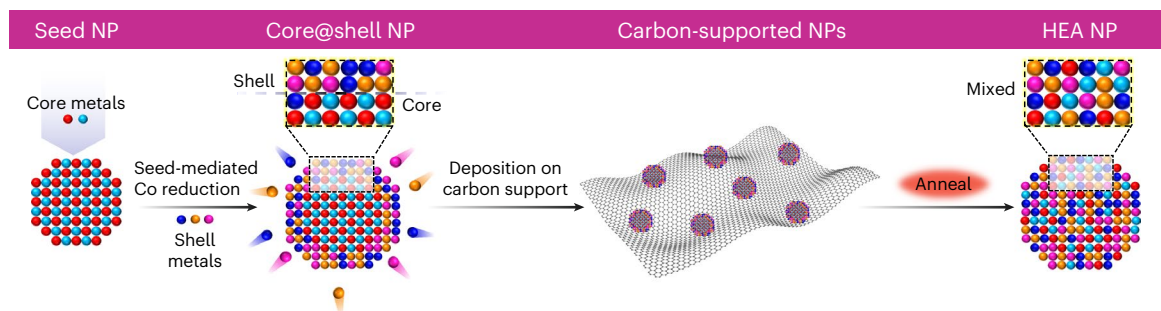


Fig. 1 | Illustration of the nanoparticle (NP) conversion process to synthesize high entropy alloy (HEA) NPs. The process starts with bimetallic seeds, then three shell metals are added as trimetallic alloy shells, creating core–shell NPs.

These core–shell NPs consisting of five metals are then dispersed on a carbon support and annealed to facilitate intermixing and the formation of HEA NPs where the five metals are mixed at the atomic level.

This demonstration of HEA NPs inspired efforts towards colloidal syntheses of HEA NPs^{8,13,14}. Such efforts are motivated by the potential to achieve greater control over NP size and shape, as well as surface ensemble sites, to enhance compatibility with different NP supports, and to accelerate understanding of nanoscale mixing behaviour. Thus far, the size dispersity of these colloidal prepared HEA NPs have not met the level of state-of-the-art monometallic or bimetallic NPs^{15–17}, with a recent mechanistic study by Schaak and co-workers showing that five metal precursors added dropwise in a heated reducing solution produced single-phased HEA NPs; however, complex intermediate phases were observed¹³. Therefore, colloidal advances will rely heavily on the practical selection of reducing agents and metal precursors to achieve other compositions of HEA NPs, which is challenging due to differences in the reduction rates of the metal precursors^{18,19}. That is, every composition may require a different reducing agent and screening of many precursor combinations^{20,21}. Here, a predictable synthetic method for HEA NPs as monodisperse samples based on a NP conversion strategy is offered²².

Organic chemistry defines the golden standard for predictable synthetic methods, where syntheses for target molecules can be designed through retrosynthetic analysis, a technique of employing chemical reactions to ‘deconstruct’ target molecules into accessible starting reagents. However, the sequential bond-breaking method applicable to organic molecules cannot be envisioned for the retrosynthesis of colloidal nanocrystals due to reaction complexity and poor understanding of reaction intermediates^{20,23}. Rather, NP conversion pathways offer a conceptually similar framework, where a target composition can be deconstructed into simpler NP components that can undergo transformation through known pathways²⁴.

Our group has previously shown the conversion of two-phase core–shell NPs into single-phase HEA NPs by thermal annealing⁹. This demonstration was achieved by preparing *i*-PdCu (*i* = intermetallic = B2) NPs for use as seeds for the deposition of trimetallic shells (Pt, Ni and M = Co, Fe, Ir, Rh or Ru) by seed-mediated co-reduction (SMCR) of multiple metal precursors⁸. This approach requires fewer metal precursors to be reduced in each step (seed synthesis and shell synthesis) compared with direct colloidal synthesis, facilitating the formation of monodisperse samples. The potentially modular nature is attractive for the retrosynthetic design of core–shell NPs as precursors to HEA NPs, where the stoichiometry of the HEA NPs is defined by the core and shell compositions and their relative volumes⁸. However, to move beyond this initial system, principles for selecting which metals go into the core versus the shell regions of the NPs become essential.

In this Article, such principles were established by considering the relative redox potentials (E_{red}) of the metal or metal precursors used in SMCR. This property is important as galvanic replacement may proceed when metal precursors with high E_{red} replace metals in

the seeds having low E_{red} ⁽²⁵⁾. Additionally, homogeneous nucleation of NPs may occur at conditions of high supersaturation or poor wetting on the seeds, generating new NPs of a different phase. Thus, three sets of experiments were designed to establish the necessary retrosynthetic design principles for core–shell NP synthesis. Once monodisperse core–shell NPs were synthesized with the requisite minimum of five metals between 5 at% and 35 at%, they were then transformed into HEA NPs via annealing, maintaining the size dispersity and well-defined composition, unlike HEA NPs produced directly by colloidal methods. Moreover, this NP conversion process is shown to be compatible with different support materials, highlighting the generality of this NP conversion strategy to HEA NPs.

Results and discussion

Incorporation of noble metals with high relative E_{red}

Figure 1 shows the sequential process involved in the formation of HEA NPs^{8,9}. For all reactions, the procedure starts with the preparation of monodisperse bimetallic seeds, which serve as the foundation for subsequent reactions. Then, in the presence of the bimetallic seeds, three metal precursors are co-reduced in a heated solution of octadecene (ODE), 1,2-dodecanediol (DDD) and oleylamine (OLA)^{26,27}. Here ODE serves as a solvent, while DDD functions as a reducing agent, and OLA fulfils both roles. The resulting core–shell NPs are then loaded onto a support and annealed at 800 °C for 2 h. Each unique combination of HEA NPs is created using the same procedure and annealing conditions.

When synthesizing core–shell NPs, galvanic replacement of the seed NPs is a commonly observed phenomenon, particularly when the seeds are composed of a metal having lower E_{red} than the anticipated shell²⁵. To mitigate galvanic replacement in SMCR, DDD is added to facilitate the reduction of metal precursors even if they have higher E_{red} compared with the seed metals. While this external reducing agent approach is effective in most cases, this experimental design may not be suitable for situations where the reduction potential difference between the seed metals and precursor metals is high (Supplementary Table 1). Specifically, efforts to add gold (M = Au) to the shell of PdCu NPs were unsuccessful when following this process. Figure 2a–e shows the characterization of the product obtained when PtBr₂, Ni(acac)₂ and AuCl were co-reduced in a heated solution of ODE, OLA and DDD in the presence of PdCu seeds of size 7.8 ± 0.4 nm, (Fig. 2a and Supplementary Fig. 1). Transmission electron microscopy (TEM) of the expected core–shell PdCu@PtNiAu NPs reveals monodisperse NPs (8.1 ± 0.6 nm) with a size comparable to the starting PdCu cores, as shown in Fig. 2b. Scanning transmission electron microscopy (STEM) interfaced with energy-dispersive X-ray spectroscopy (EDS) elemental mapping and linescan analysis show the spatial distribution of the metals in these NPs. The NPs show strong signals of Au, Pt and Ni with variation in at% from one NP to another and no evidence of a core–shell architecture (Fig. 2c,d). Elemental analysis by scanning electron microscopy

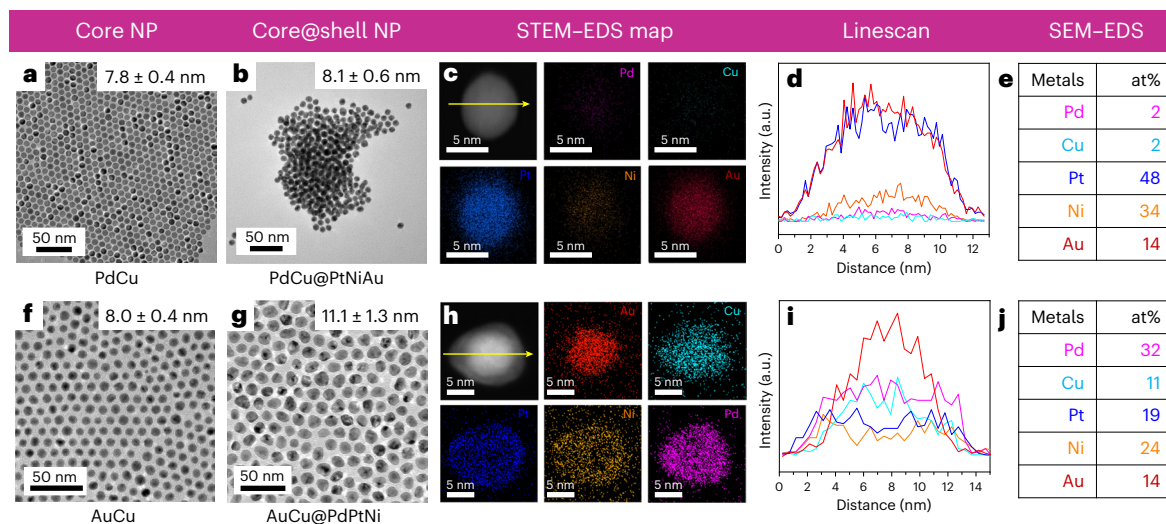


Fig. 2 | Characterization of Au-containing NPs. **a–e**, Transmission electron microscopy (TEM) image of PdCu NPs (**a**) as well as TEM image (**b**), scanning transmission electron microscopy coupled with energy-dispersive X-ray spectroscopy (STEM–EDS) elemental maps (**c**), linescan analysis (**d**) and table with compositional information (atomic percentage, at%) from SEM–EDS of

product from seed-mediated co-reduction (SMCR) with PdCu NPs and Pt, Ni, and Au precursors (**e**). **f–j**, TEM image of AuCu NPs (**f**) as well as TEM image (**g**), STEM–EDS elemental map (**h**), linescan analysis (**i**) and table with compositional information from SEM–EDS of AuCu@PdPtNi NPs (**j**).

(SEM)–EDS shows the at% of Au, Pt and Ni are higher than the Pd and Cu, shown in Fig. 2e and Supplementary Fig. 2. The NPs were characterized by powder X-ray diffraction (XRD) revealing no reflections corresponding to the PdCu phase (Supplementary Fig. 3). Pd and Cu depletion is in stark contrast to our earlier report⁸ of other PdCu@PtNiM NPs where all five metals were nearly in equal amounts; this observation suggests that the high E_{red} of the Au precursor compared with Pd and Cu may be facilitating galvanic replacement (Supplementary Table 1)^{28,29}.

To investigate this observation further, only AuCl was used as a metal shell precursor and reduced in the presence of PdCu seeds with OLA, ODE and DDD. Monodisperse NPs were obtained with a size of 9.0 ± 0.8 nm (Supplementary Fig. 4a). XRD shows a reflection consistent with the PdCu phase, along with additional reflections for a Pd–Au alloy (Supplementary Fig. 4b). From STEM–EDS elemental mapping, the PdCu domain is smaller (~ 3 nm) than the initial PdCu seeds (~ 8 nm). The linescan shows the Pd and Cu signals are localized in the low Au signal region (Supplementary Fig. 4c,d). Similar results of Pd and Cu signal depletion and Pd–Au alloy phase formation were observed with other Au precursors that were typically used for colloidal Au NPs synthesis, for example Au(ac)₃ and HAuCl₄·3H₂O (Supplementary Figs. 4e, 5a–c and 6a–c). In the case of HAuCl₄·3H₂O, the Au signal can be seen all over the NPs in STEM–EDS rather than to one side like AuCl and Au(ac)₃ experiments (Supplementary Figs. 5d and 6d). The Pd:Cu:Au at% deviated from the expected at% ratio of 1:1:1, again supporting that galvanic replacement is occurring (Supplementary Figs. 5e and 6e). Adding either Ni(acac)₂ or PtBr₂ along with the AuCl precursor gave a product with similar Au and Cu signal segregation by STEM–EDS elemental mapping and linescan profiles (Supplementary Figs. 7 and 8). Notably, in both cases, decreases in the PdCu domain sizes are observed and characteristic of galvanic replacement. Overall, these experiments support that galvanic replacement is occurring with precursors with a high E_{red} relative to the seed metals (Supplementary Table 1) even though the synthetic system does have a suitable molecular reducing agent for shell deposition²⁹. We note that all the precursors were chosen on the basis of their ready availability and good solubility in the OLA and ODE media.

From the perspective of retrosynthetic design, these results indicate that metal salts with high E_{red} compared with seed metals will facilitate galvanic replacement and inhibit the formation of the target

core–shell NPs. Thus, rather than adding such metals to the shell by SMCR, such metals are better suited for the core. To demonstrate this concept, synthetically accessible AuCu NPs were used as seeds with SMCR of Pd, Pt and Ni salts to create core–shell AuCu@PdPtNi NPs. Figure 2f–j shows the characterization of the core–shell AuCu@PdPtNi NPs. Monodisperse alloy AuCu NPs of size 8.0 ± 0.4 nm (Fig. 2f and Supplementary Fig. 9) were synthesized using a prior reported colloidal process³⁰. These NPs were then used as seeds with PdBr₂, PtBr₂ and Ni(acac)₂ being co-reduced in the SMCR stage. The TEM image in Fig. 2g shows the obtained core–shell NPs have a size distribution of 11.1 ± 1.3 nm with a size increase from the starting AuCu NPs. The XRD pattern of the AuCu@PdPtNi NPs has an asymmetric (111) reflection, which can be indexed to the AuCu alloy phase (the shoulders at lower 2θ) and a random alloy face-centred cubic (FCC) phase for the PdPtNi shell. The PdPtNi alloy shell peak positions are in agreement with the anticipated alloy reference, which was calculated on the basis of the elemental ratios of the shell determined by SEM–EDS and Vegard's law (Supplementary Fig. 10)³¹. STEM–EDS shows that Au and Cu signals are located at the centre of the NPs, whereas the Pt, Ni and Pd signals are distributed at the exterior of the NPs, supporting a core–shell architecture (Fig. 2h,i). We note that the Cu signal spreads over a greater area than Au in the STEM–EDS map, which may arise from initial galvanic replacement of Cu from the seeds by the metal precursors followed by redeposition of Cu in the presence of the reducing agents (which could result in alloying with shell metals). After initial galvanic replacement, the surface becomes Au rich, which would hinder further galvanic replacement of Cu. The composition of the core–shell AuCu@PdPtNi NPs evaluated by SEM–EDS indicates the co-existence of Au and all the other anticipated metals (Fig. 2j and Supplementary Fig. 11). These studies suggest that metals with high E_{red} should be contained within the cores whenever possible.

Susceptibility of seeds to galvanic replacement as per E_{red}

To test this emerging design criterion further and better understand core–shell NP formation requirements based on E_{red} of the target metals, three Pd-based bimetallic cores were selected (PdAg, PdCu and PdCo), where Ag has the highest E_{red} followed by Cu then Co. Based on the E_{red} values (Supplementary Table 1), the PdCo NPs were hypothesized to undergo galvanic replacement to a greater extent compared with the PdCu NPs, with the PdAg NPs anticipated to undergo the least

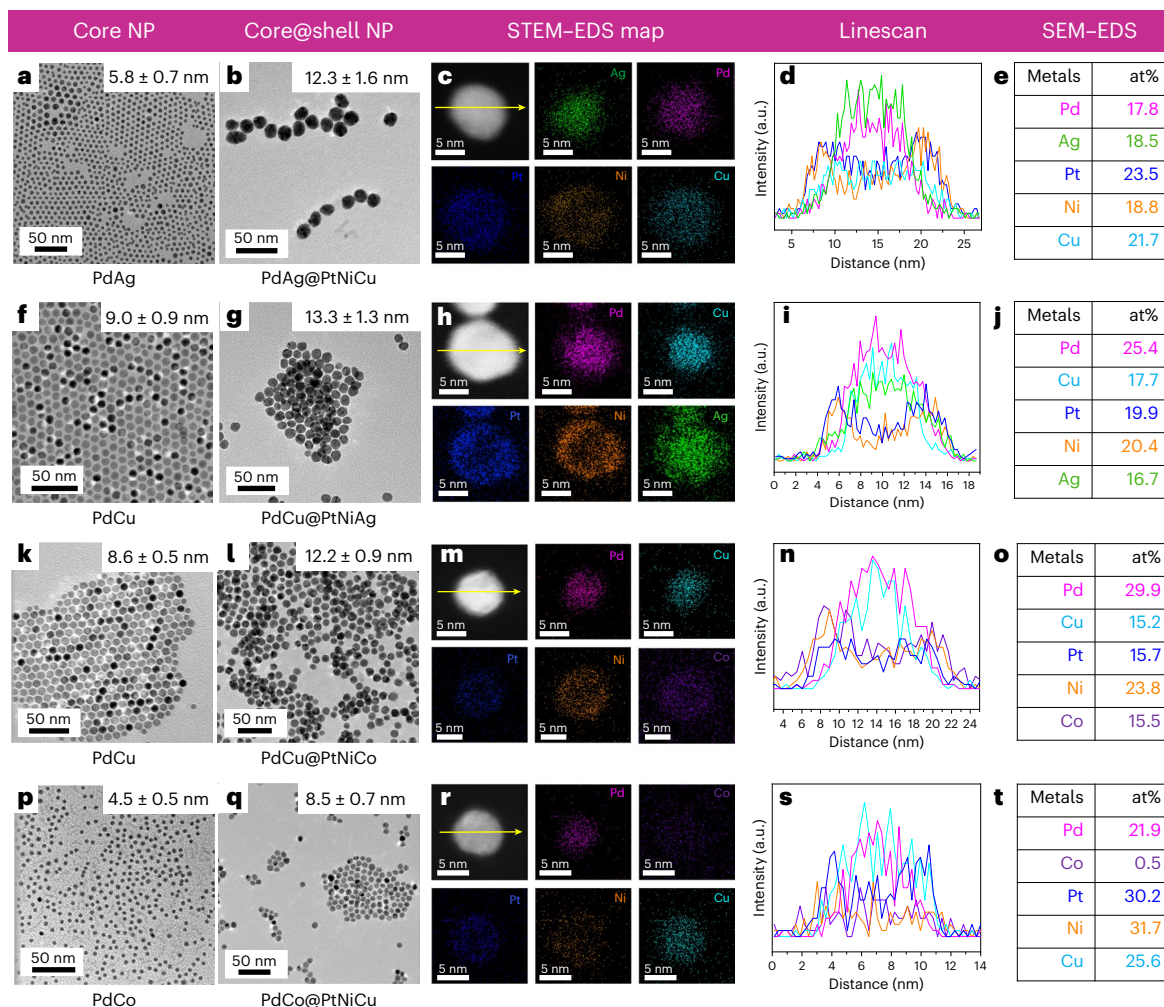


Fig. 3 | Characterization of NPs from redox potential (E_{red}) reactivity study. **a–e**, TEM image of PdAg seeds (**a**) and TEM image (**b**), STEM–EDS elemental map (**c**), linescan analysis (**d**) and table of compositional information from SEM–EDS of product targeting PdAg@PtNiCu NPs (**e**). **f–j**, TEM image of PdCu NPs (**f**) as well as TEM image (**g**), STEM–EDS elemental map (**h**), linescan analysis (**i**) and table with compositional information from SEM–EDS of targeting

PdCu@PdNiAg NPs (**j**). **k–o**, TEM image of PdCu NPs (**k**) as well as TEM image (**l**), STEM–EDS elemental map (**m**), linescan analysis (**n**) and table with compositional information from SEM–EDS of PdCu@PdNiCu NPs (**o**). **p–t**, TEM image of PdCo NPs (**p**) as well as TEM image (**q**), STEM–EDS elemental map (**r**), linescan analysis (**s**) and table with compositional information from SEM–EDS of PdCo@PtNiCu NPs (**t**).

amount of galvanic replacement during SMCR to deposit trimetallic shells. Figure 3 shows the characterization of the products from these experiments.

In the first system, alloy PdAg NPs of size 5.8 ± 0.7 nm (Fig. 3a and Supplementary Fig. 12a) were synthesized following a previous report³² and size separated as some PdAg NPs were observed to fuse together (Supplementary Fig. 12b–d). Then, shell metal precursors PtBr₂, Cu(ac)₂ and Ni(acac)₂ were co-reduced in the presence of the PdAg seeds. TEM images show core–shell PdAg@PtNiCu NPs of diameter 12.3 ± 1.6 nm as the majority product (Fig. 3b); the larger than anticipated size increase (typically 1–2 nm versus 3–3.5 nm) is probably due to NP fusion. This observation does not, however, limit our ability to evaluate the extent to which galvanic replacement may be occurring. STEM–EDS elemental mapping and linescan analysis show that Pd and Ag signals are contained in the centres and Pt, Cu and Ni signals in the exteriors of the NPs (Fig. 3c,d). The composition of the core–shell PdAg@PtNiCu NPs evaluated by SEM–EDS indicates that all five metals are present within the range 18–24 at% (Fig. 3e and Supplementary Fig. 13). The XRD pattern shows one broad asymmetric (111) reflection for PdAg core and PtNiCu shell (Supplementary Fig. 14). The finding is consistent with core–shell NP formation and is unsurprising as the metals Pd and Ag have either higher than or comparable

E_{red} to the metal precursors (PtBr₂, Cu(ac)₂ and Ni(acac)₂) added in the SMCR process. We note that PtBr₂ could participate in galvanic replacement, although its participation would be hindered with the use of the external reducing agent.

In contrast, galvanic replacement was observed to some extent while attempting to prepare core–shell PdCu@PtNiAg NPs as the Ag precursor has a higher E_{red} than the core metal, Cu. Figure 3f–j shows the characterization of the NPs from this synthesis. First, monodisperse 9.0 ± 0.9 nm sized PdCu NPs were synthesized (Fig. 3f) and used for the SMCR step where AgBr was used as a Ag precursor along with the same Pt and Ni precursors as before. TEM images of the product NPs confirm a size of 13.3 ± 1.3 nm (Fig. 3g), and SEM–EDS confirms the presence of all the anticipated metals, ranging from 17 at% to 25 at% (Fig. 3j and Supplementary Fig. 15). STEM–EDS elemental distribution and linescan analysis show the Ag signal is observed throughout the NPs and higher in their centre (Fig. 3h,i). This Ag signal in the centre of the core–shell NPs when compared with the PdCu@Au system suggests that migration of noble metal inside the NPs is occurring through galvanic replacement. XRD shows that the i-PdCu phase is maintained by the peak at 30° (Supplementary Fig. 16), which suggests that the extent of Pd and Cu replacement is not as high as when attempting to synthesize PdCu@PtNiAu NPs.

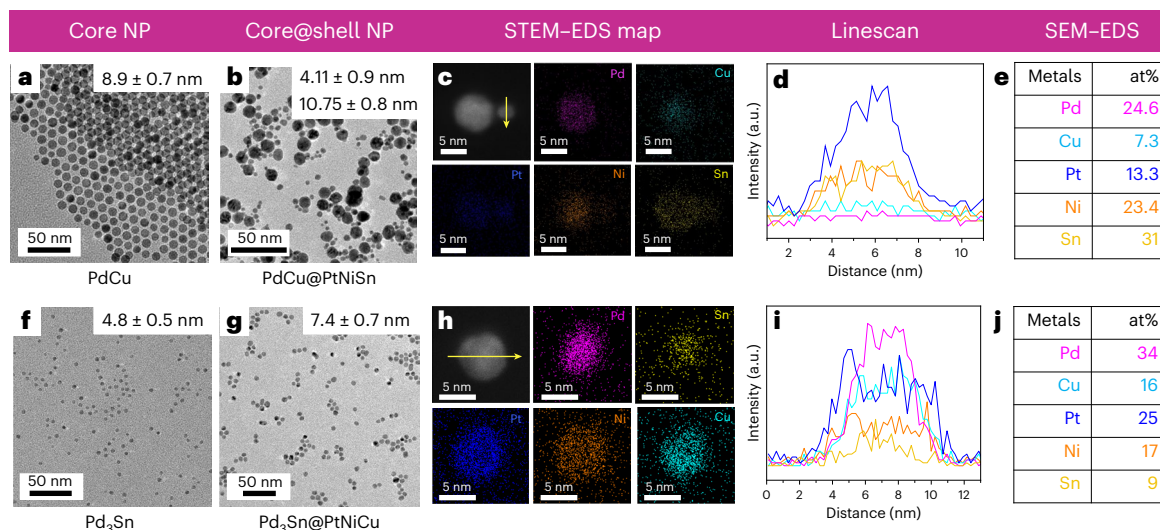


Fig. 4 | Characterization of Sn-containing NPs. **a–e**, TEM image of PdCu NPs (**a**) and TEM image (**b**), STEM–EDS elemental map (**c**), linescan analysis (**d**) and table of compositional information from SEM–EDS of product from SMCR with PdCu

seeds and Pt, Ni and Sn precursors (**e**). **f–j**, TEM image of Pd₃Sn NPs (**f**) and TEM image (**g**), STEM–EDS elemental map (**h**), linescan analysis of smaller NPs (**i**) and table of compositional information from SEM–EDS of Pd₃Sn@PtNiCu NPs (**j**).

Interestingly, when the Ag precursor is replaced with a Co precursor, Co(ac)₂·4H₂O (Co²⁺ to Co has a low E_{red} compared with Ag⁺/Ag as shown in Supplementary Table 1), the targeted core–shell PdCu@PtNiCo NPs form and no galvanic replacement was evident. These core–shell NPs were prepared from PdCu cores of similar size (Fig. 3k) as before and then PtBr₂, Co(ac)₂ and Ni(acac)₂ were used for shell formation. TEM images show the monodispersity of the spheroidal PdCu@PtNiCo NPs with a size of 12.2 ± 0.9 nm (Fig. 3l). XRD shows two sets of peaks, one for core and one for shell (Supplementary Fig. 17). The STEM–EDS indicates the formation of core–shell NPs as the Pd and Cu signals are higher in the centres of the NPs and Pt, Ni and Co signals are higher at the outer sides of the NPs (Fig. 3m,n). SEM–EDS also shows the presence of all five metals in the NPs (Fig. 3o and Supplementary Fig. 18). Comparing these results with when PdCu seeds are used with SMCR to deposit trimetallic shells containing either Au or Ag (Fig. 2a–e and Fig. 3f–j), a reactivity trend is evident. Specifically, due to its high E_{red} , the Au precursor tends to replace large portions of the core metals via galvanic replacement, while the Ag precursor exhibits lower reactivity than that (Supplementary Table 1). Notably, no galvanic replacement is observed for the Co redox pair (Supplementary Table 1), which is the least reactive.

Finally, a substantial amount of galvanic replacement was observed when targeting core–shell PdCo@PtNiCu NPs as shown in Fig. 3p–t. Specifically, alloy PdCo cores (Pd₆₅Co₃₅ Pd:Co at% ratio from 65:35), measuring 4.5 ± 0.5 nm in size were prepared by a previously reported process³³ (Fig. 3p and Supplementary Fig. 19), and PtBr₂, Ni(acac)₂ and Cu(ac)₂ were simultaneously reduced in the presence of the PdCo seeds. Elemental analysis by SEM–EDS shows that the at% of Pd, Pt, Ni and Cu metal varies between 22 at% and 32 at%. The at% of Co is found to be 0.5%, which is much less than the expected Co amount of 12 at% based on the original seed composition (Fig. 3t and Supplementary Fig. 20). XRD shows no asymmetric or separate reflections for the PdCo seeds (Supplementary Fig. 21). The STEM–EDS elemental map and linescan show that the Pd and Cu signals in the centres and Ni, Pt signals are strongest at the exteriors of the NPs (Fig. 3r,s). Low Co signal as background noise is observed from the TEM instrument condenser apparatus. Here, the E_{red} for Co²⁺/Co, as indicated in Supplementary Table 1, is –0.277 V versus SHE lower compared with Cu^{x+}/Cu^{y+} ($x = 2/1, y = 1/0$). This larger difference in E_{red} between Co and Pt in the case of PdCo, compared with E_{red} between Cu and Pt in the case of PdCu, promotes galvanic replacement to a

greater extent in the PtCo system, facilitating the oxidation of Co from the seeds.

These results are consistent with the initial hypothesis that galvanic replacement reactivity is high in the case of PdCo, then PdCu, and finally PdAg NPs. From these systematic comparisons, we can predict in a retrosynthetic manner that metals with a high E_{red} should go into the core, and metals having low E_{red} should go into the shell of core–shell NPs. More broadly, the relative redox properties of the metals in the target HEA NPs need to be considered.

Homogeneous versus seeded nucleation

Beyond galvanic replacement, newly formed NPs can form through homogeneous nucleation and be a hurdle during the synthesis of core–shell NPs. Homogeneous nucleation can be favoured even in the presence of NP seeds when surface wettability on the seeds is unfavourable (such as with large lattice mismatch systems or strongly bound capping ligands) or when conditions favour high supersaturation. To study this effect, the addition of Sn to the core–shell NPs was considered. The low E_{red} of Sn²⁺/Sn (Supplementary Table 1) leads to the prediction that PdCu seeds will not undergo replacement (galvanic replacement), nor should homogeneous nucleation occur due to high supersaturation. However, Pd, Pt, Cu, Ni, Au, Ag and Co adopt an FCC phase, but the stable allotrope of Sn adopts a body-centred tetragonal crystal structure³⁴. This feature can hinder shell formation due to a large lattice mismatch between seeds and shells and because alloys are favoured when the crystal structures of the metals are similar. Nonetheless, oxophilic Sn and other p-block elements can play a vital role in making alloy NPs electrochemically active^{35,36}. Therefore, the incorporation of Sn in the HEA NPs would not only represent a p-block element but also serve as a desirable metal for future catalysis.

Considering the features of Sn, the inability to synthesize core–shell PdCu@PtNiSn NPs with standard SMCR conditions is unsurprising. Figure 4a–e show the characterization of the product produced when SnCl₂ was used as a metal precursor along with PtBr₂ and Ni(acac)₂ in the SMCR step in the presence of PdCu seeds (Fig. 4a). SnCl₂ is a commonly used reagent for the synthesis of NPs made of Sn^{37,38}. After the SMCR step, NPs (Fig. 4b, average size of 4.11 ± 0.9 nm) smaller than the initial PdCu seeds of 8.9 ± 0.7 nm (Fig. 4a) were observed rather than NPs with increased size. Along with smaller NPs, larger particles having size of 10.75 ± 0.8 nm were also observed. The XRD pattern shows an asymmetric peak around 40° and a peak around 30° supporting PdCu phase with new phases (Supplementary Fig. 22). The STEM–EDS

mapping and the linescan of the smaller NPs show the NPs consist of predominantly Sn, Ni and Pt metals (Fig. 4c,d). The larger NPs show an uneven distribution of all five metals and no core-shell architecture (Supplementary Fig. 23). The composition of the resulting NPs evaluated by SEM-EDS indicates that all the metals are present (Fig. 4e and Supplementary Fig. 24). However, this composition analysis is an average of the two distributions of NPs. In this SMCR process, the Sn precursor (SnCl_2) undergoes reduction, with homogeneous nucleation observed along with some uneven heterogeneous nucleation and growth on the PdCu NPs. This observation suggests that metals with unfavourable wetting behaviour for shell formation should go into the core of the core-shell NPs.

Therefore, Sn was incorporated in the core NPs instead. Pd_3Sn NPs were selected for their high monodispersity and quasi-spherical shape as PdSn NPs with a 1:1 ratio are synthetically challenging to access as monodisperse samples³⁹. They are shown in Fig. 4f, with a size of 4.8 ± 0.5 nm. The phase of the Pd_3Sn NPs is inconclusive because the disordered and ordered phases of Pd_3Sn are nearly identical (Supplementary Fig. 25). Shell metal precursors of PtBr_2 , $\text{Ni}(\text{acac})_2$ and $\text{Cu}(\text{ac})_2$ were co-reduced in the presence of the Pd_3Sn seeds, producing NPs with an average size of 7.4 ± 0.7 nm (Fig. 4g). The XRD pattern matches well with the calculated shell alloy peak (Supplementary Fig. 26). STEM-EDS elemental mapping and linescan profile show that Pd and Sn signals are located at the centres of the NPs, whereas the Pt, Ni and Cu are distributed on the external parts of the NPs, which is consistent with a core-shell architecture (Fig. 4h,i). We note that Cu forms uneven shells, leading to different STEM-EDS mapping results depending on the orientation of the core-shell NPs (Supplementary Fig. 27). The Sn signal is low due to the stoichiometry of the Pd_3Sn cores where Pd:Sn at% ratio was close to 3:1. The composition of the NPs evaluated by SEM-EDS indicates the co-existence of all metals within the range of HEA definition 5–35 at% (Fig. 4j and Supplementary Fig. 28).

These studies show that for metals where homogeneous nucleation may be favoured either due to synthetic conditions that generate high supersaturation or poor wetting behaviour, such metals should go into the core of the core-shell NPs.

Conversion of core-shell NPs to monodisperse HEA NPs

The core-shell NPs mentioned previously were converted to HEA NPs. AuCu@PdPtNi , PdAg@PtNiCu , PdCu@PtNiCo and $\text{Pd}_3\text{Sn@PtNiCu}$ NPs were used to make monodisperse HEA NPs by thermal-induced diffusion. First, the core-shell NPs were distributed on a carbon support (ketjen) to keep the NPs well separated as the high annealing temperatures will degrade the capping agents used in their synthesis, and NP coalescence, aggregation and sintering could happen at high loadings⁴⁰. The supported core-shell NPs were heated at 800 °C for 2 h under a flow of H_2/N_2 (4 v/v%) mixed gas. Figure 5 shows characterizations of the resultant HEA NPs.

For the AuCuPdPtNi HEA NPs (Fig. 5a–e), the size distribution of the HEA NPs was 13.4 ± 1.5 nm (Fig. 5a), which shows that the monodispersity of the initial core-shell AuCu@PdPtNi NPs (size 11.1 ± 1.3 nm) is transferred to the AuCuPdPtNi HEA NPs. We note minor deviations in the size of the HEA NPs, which may be from the slightly uneven height of the core-shell NPs when dispersed on the carbon. The high-resolution TEM micrographs show the lattice fringes corresponding to 0.24 nm of the (111) and further support the formation of single-phase and single-crystalline AuCuPdPtNi HEA NPs (Supplementary Fig. 29). The XRD shows a single set of reflections that do not match the pure metals (Au, Cu, Pt, Ni or Pd) or the precursor core-shell NPs, supporting formation of a single-phase alloy (Supplementary Fig. 30). The predicted XRD pattern using Vegard's law agrees with the AuCuPdPtNi XRD pattern (Fig. 5d). The elemental mapping and linescan support the complete mixing of the five metals within the individual NPs, but STEM-EDS is a 2D projection of a 3D distribution so some intraparticle heterogeneity may not be evident from analysis (Fig. 5b,c and Supplementary Fig. 31)⁸.

X-ray photoelectron spectroscopy (XPS) shows atomic percentages of Au (20 at%), Cu (21 at%), Pt (16 at%), Ni (13 at%) and Pd (29 at%) (Fig. 5e). We note that the metal concentrations are not precisely equivalent to 1:1:1:1:1 at%; instead, they range from 5 at% to 35 at%, which is necessary for establishing a general proof of concept. The binding energies obtained from XPS analysis for the predominant features of each metal demonstrate close agreement with typical metallic values (Supplementary Fig. 32). We note that light surface metal enrichment (Pd signal in the Fig. 5c STEM-EDS linescan) was observed, which supports surface segregation corroborated by molecular dynamics simulations⁸.

Considering the synthesis of HEA NPs further, the carbothermal shock technique discussed in the introduction requires immobilization on supports, much like our NP conversion strategy. However, the carbothermal shock method is only compatible with electrically conductive supports^{12,41}, but different supports may be required for the application of HEA NPs. Thus, in addition to the carbon support, the core-shell AuCu@PdPtNi NPs were also dispersed on titania (titanium oxide) and annealed under comparable conditions to achieve monodisperse AuCuPdPtNi HEA NPs (Supplementary Fig. 33), demonstrating the versatility of this NP conversion method¹².

In a similar process, the core-shell $\text{Pd}_3\text{Sn@PtNiCu}$ NPs were annealed, forming PdSnPtNiCu HEA NPs on carbon with a size of 7.5 ± 1.0 nm (Fig. 5f). High-resolution TEM supports the formation of single-phase, single-crystalline NPs (Supplementary Fig. 34). The STEM-EDS elemental mapping images and linescan profile support complete mixing of the five metals within the individual NPs (Fig. 5g,h). The XRD profile shows a single set of reflections that do not match with the pure Pd, Sn, Pt, Ni and Cu or the precursor core-shell NPs, supporting the formation of a single-phase alloy without any phase segregation (Supplementary Fig. 35). The XRD peaks are also in reasonable agreement with the calculated XRD pattern using Vegard's law, (Fig. 5i)³⁹ where the lattice parameter from a simulated fcc Sn structure was used to calculate the predicted XRD pattern for PdSnPtNiCu NPs³⁴. It is worth mentioning that the slightly uneven shape of the shell (in this case, Cu) does not seem to have an impact during the annealing process. XPS shows a surface at% of Pd (26 at%), Sn (9 at%), Pt (23 at%), Ni (19 at%) and Cu (23 at%) (Fig. 5j and Supplementary Fig. 36).

The conversion of core-shell PdAg@PtNiCu and PdCu@PtNiCo NPs also results in monodisperse PdAgPtNiCu NPs shown in Fig. 5k–o of size 13.8 ± 1.5 nm (Fig. 5k) and PdCuPtNiCo NPs shown in Fig. 5p–t of size 12.1 ± 2.4 nm (Supplementary Figs. 37 and 38). The mixture of five different metals is depicted by the STEM-EDS with linescan (Fig. 5l,m,q,r). Furthermore, one set of FCC reflections are visible in XRD (Fig. 5n,s), matching well with the calculated patterns (Supplementary Figs. 39 and 40). The at% obtained by XPS demonstrates adequate agreement with the core-shell starting point (Fig. 5o,t and Supplementary Figs. 41, and 42). Overall, from NPs with four different cores, monodisperse HEA NPs of various metal compositions were synthesized.

Additional mechanistic studies were conducted to investigate the intermediates that form when heating core-shell PdCu@PtNiCo NPs before fully mixed PdCuPtNiCo HEA NPs form. The core-shell PdCu@PtNiCo system was chosen because of the distinct reflections in XRD for the PdCu B2 core and PtNiCo shell. XRD shows a gradual transition in XRD peaks, shifting from core-shell NPs (exhibiting two reflections, one corresponding to the core phase and one corresponding to the shell phase) to HEA NPs (displaying a single reflection consistent with the HEA phase) (Supplementary Fig. 43a) as the carbon supported sample is heated from room temperature to 600 °C. In this study, the maximum temperature is limited to 600 °C, which was sufficient for producing HEA NPs of this composition⁹. STEM-EDS data and the linescans for NPs heated to 300, 400, 500 and 600 °C show varying degrees of core and shell phase mixing compared with the original core-shell NPs (Supplementary Fig. 43b–g). This ability to manipulate the degree of intermixing is important to the potential catalytic applications of HEA NPs as there is tremendous interest in achieving different

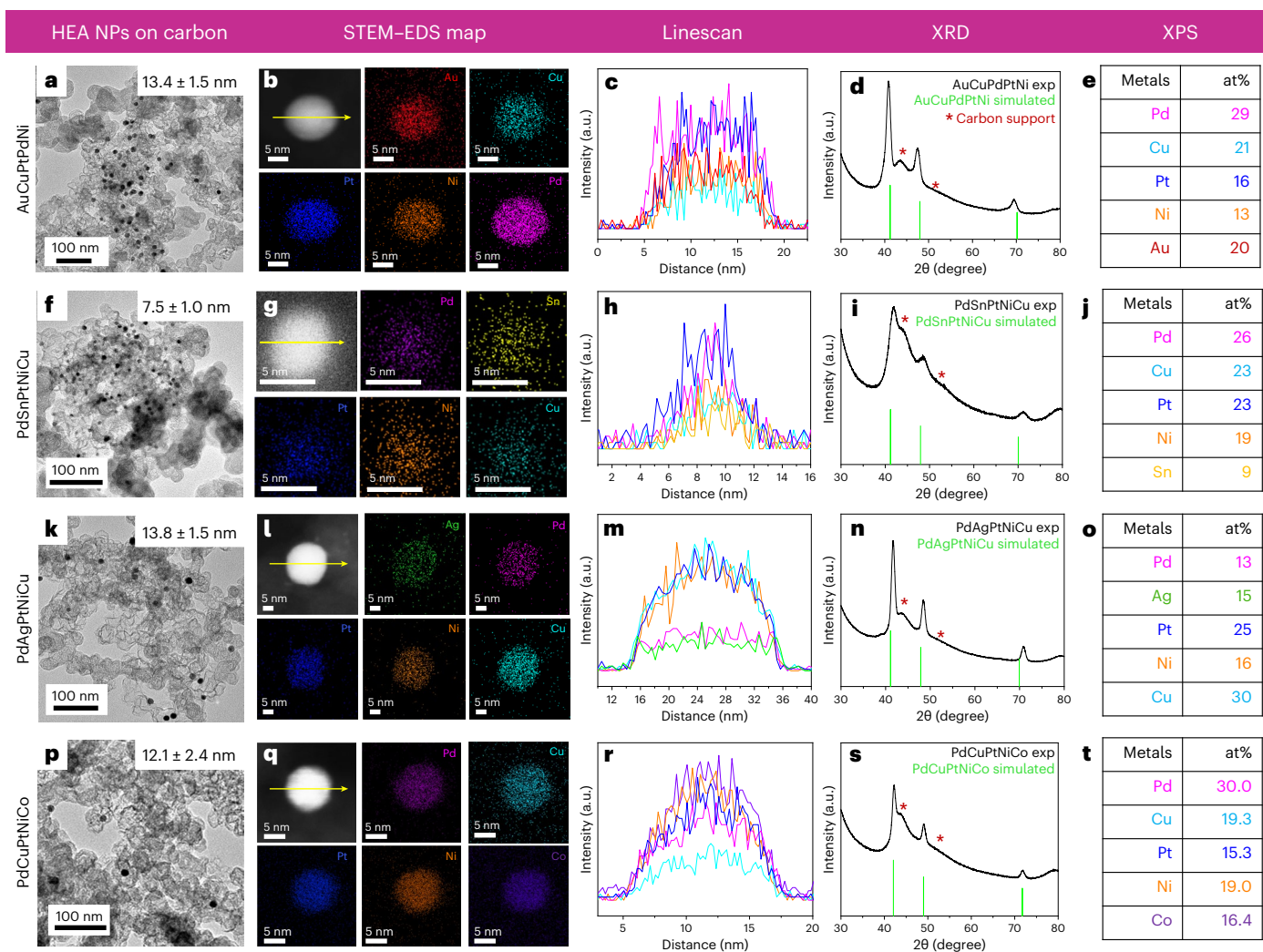


Fig. 5 | Morphological and compositional characterization of monodisperse HEA NPs. **a–t**, TEM images (**a**, **f**, **k** and **p**), STEM-EDS elemental mapping (**b**, **g**, **l** and **q**), linescan analysis according to yellow lines (**c**, **h**, **m** and **r**), X-ray diffraction (XRD) pattern (**d**, **i**, **n** and **s**) and table showing the atomic percentages taken by

X-ray photoelectron spectroscopy (XPS) (**e**, **j**, **o** and **t**) of the samples AuCuPtPdNi (**a–e**), PdSnPtNiCu (**f–j**), PdAgPtNiCu (**k–o**) and PdCuPtNiCo (**p–t**). XRD of alloy references were calculated by considering the elemental composition by XPS and Vegard's law.

surface ensemble sites and interfacial configurations⁴³ and has not been readily demonstrated by most HEA NP synthetic techniques.

The near equimolar ratio of metals in the core-shell NPs increases the mixing entropy of the system, thereby stabilizing the solid solution rather than phase-segregated NPs (Supplementary Note 1). Moreover, the high annealing temperature overcomes the barrier to diffusion to facilitate core metals to diffuse into the outer portion of the NPs and vice versa (Supplementary Note 2). If shape control of future HEA NPs is possible via this NP conversion route, detailed knowledge of the mixing behaviour is essential and should be possible by the strategy outlined in Supplementary Fig. 43. These experiments demonstrate that the core-shell NP conversion strategy to monodisperse HEA NPs can be generalized establishing a new paradigm for material synthesis.

Conclusion

A general conversion strategy for synthesizing monodisperse HEA NPs has been demonstrated, with retrosynthetic design principles for the design of monodisperse core-shell precursor NPs being established. These principles include: (1) metal precursors that have a high E_{red} relative to other constituent metals should be incorporated in the core of the core-shell NPs, (2) metal precursors that have a much lower E_{red} relative to the other constituent metals should go in the shell, (3) metals

that are adverse to alloy phase formation or have poor wettability should go in the core of the core-shell NPs. These syntheses should be done with additional considerations that include: (1) the starting NP seeds should be monodisperse, (2) the local ligand environment of the NP seeds as well as the shell metal precursors may influence whether or not shell deposition is favourable, and (3) the stoichiometry of the HEA NPs will be defined by the individual compositions of the seeds and shells and (4) the ratio set by the seed:shell volume⁸. The annealing process shows its applicability for different NP supports, such as conductive ones like ketjen carbon and non-conductive ones like titania, and also allows for the degree of intermixing between the core and shell phases to be controlled, tuning metal ensemble sites in the HEA NPs systems. We view this NP conversion strategy to HEA NPs as highly modular, providing a pathway to obtain size-tunable monodisperse samples with a wide range of compositions.

Methods

Chemicals

Palladium (II) bromide (PdBr_2), copper (II) acetate ($\text{Cu}(\text{ac})_2$), platinum (II) bromide (PtBr_2), nickel (II) acetylacetonate ($\text{Ni}(\text{acac})_2$), cobalt (II) acetylacetonate ($\text{Co}(\text{acac})_2$), tin (II) acetate ($\text{Sn}(\text{ac})_2$), tetrachloroauric(III) acid trihydrate ($\text{HAuCl}_4 \cdot 3\text{H}_2\text{O}$), gold (I) chloride

(AuCl), tin (II) chloride (SnCl₂), silver (I) bromide (AgBr), silver (I) nitrate (AgNO₃), oleylamine (OLA 70% O7805 and >70% 909831), oleic acid (90%, OA), trioctylphosphine (97%, TOP), 1,2-dodecanediol (90%, DDD), isopropyl alcohol (IPA) and 1-octadecene (90%, ODE) were purchased from Sigma-Aldrich. Gold (III) acetate (Au(ac)₃), titanium (IV) oxide or titania, and Aeroxide(R) P25 (Evonik brand) were purchased from Alfa Aesar, by Thermo Fisher Scientific. Ketjenblack EC-300JD was bought from Fuel Cell Store. Hexane, ethanol, acetone and isopropanol were of analytical grade. All chemicals were used without further purification. All syntheses were carried out using a vacuum/dry argon (Ar) Schlenk line. All glassware was washed with aqua regia and then distilled water numerous times.

Characterization

TEM images of NPs were taken on a JEOL 1400Plus transmission electron microscope operating at 120 keV, and images were collected with a CMOS camera (Oneview camera, Gatan). STEM-EDS images were collected with JEOL JEM 3200FS microscope operating at 300 keV using a 4k × 4k Gatan UltraScan 4000 CCD camera. The JEOL JEM 3200FS was interfaced with an Oxford Silicon Drift Detector for EDS. All samples for TEM and STEM imaging were prepared by dropcasting ~10 μl of solution onto carbon-coated Cu, Ni, Au and Mo grids (Formvar/Carbon 200 mesh Ted Pella). The grids are picked to ensure that the grid metal and metallic constituent of the analysed NPs do not match.

The atomic percentages were determined by SEM-EDS over a sample area of at least 10 μm² (a large number of NPs) with Zeiss Auriga 60 FIB-SEM equipped with the X-Max 50 mm² silicon drift detector and the AZtec software package (Oxford Instrument).

The powder X-ray diffraction (XRD or PXRD) patterns were collected on a PANalytical Empyrean instrument (operated at 40 kV and 45 mA) with Cu Kα radiation with a wavelength of 1.5418 Å and an X'Celerator linear strip detector. Samples for XRD were prepared by dropcasting NPs solutions onto single crystalline Si substrates.

XPS measurements were collected using a PHI 5000 Versa Probe II equipped with a focused monochromatic Al Kα X-ray source. A beam size of 100 μm and an X-ray power of 50 W at 15 keV under ultrahigh vacuum conditions were used for all experiments. Binding energies were calibrated by assigning the C 1s peak to 284.8 eV.

The sizes of the NPs were determined using an automated MATLAB code measuring the contrast difference between the NPs and the background; more information can be found in the work reported by Harak et al.⁴⁴. Some NPs were measured manually in ImageJ or Fiji. More than 100 NPs are measured to calculate the standard deviations in size.

Synthesis of i-PdCu (i or intermetallic or B2) NPs

The i-PdCu NPs were synthesized as previously described by the Skrabalak group^{8,9}. To a 100 ml round-bottom flask (RBF), 36 mg of Cu(ac)₂, 54 mg of PdBr₂, 18 ml of OLA and 40 μl of OA were added, and this mixture was heated under vacuum to 110 °C with a heating mantle and held for 10 min with stirring. Then, 60 μl of TOP was added, and the solution was heated to 235 °C under Ar and held at this temperature for 30 min. Then, the solution was cooled to 70–80 °C and 40 ml of hexane was added. Then the total solution was separated into two centrifuge tubes and centrifuged at 2,050g for 10 min to remove any large particles. The rest of the particles (contained in the collected supernatant) were precipitated by adding a mixture of 3:1 acetone/ethanol, followed by collection by centrifugation at 11,404g for 10 min. The obtained particles were centrifuged again at 11,404g for 10 min with a mixture of ethanol and hexane (5:1 vol). After removal of the supernatant, the particles were finally resuspended in 3 ml of hexane and 16 ml of a solution of acetone/methanol 2:1 for storage.

Synthesis of AuCu NPs

The AuCu NPs were synthesized by a modified procedure previously described by the Skrabalak group³⁰. To a 100 ml RBF, 20.0 mL of ODE

was added and was heated under a vacuum to 130 °C and held for 30 min while stirring. In a glass scintillation vial, 5 ml of OLA (70% O7805), 0.12 mmol Au(ac)₃ and 0.22 mmol Cu(ac)₂ were heated at 90 °C while stirring until the metal precursor was dissolved. The OLA solution was added to the RBF along with 2.47 mmol 1,2-dodecanediol and 5.1 ml of OA. The solution was heated to 165 °C under Ar and was maintained at this temperature for 90 min. Then, the solution was cooled until 70–80 °C and 40 ml of hexane was added. Then the total solution was separated in two centrifuge tubes and centrifuged at 2,050g for 10 min to remove any large particles. Fifteen millilitres of ethanol was added to the supernatants of each of the centrifuge tubes. The tubes were centrifuged at 11,404g for 10 min. The supernatants were discarded and the pellets were combined in a new centrifuge tube with the help of 3 ml of hexane. At this stage, size centrifugation was performed. With the 3 ml of dispersion, 20 ml of hexane was added along with 4 ml of acetone. The tube was centrifuged at 11,404g for 10 min. The pellet from this washing step will contain larger NPs and thus stored with 3 ml hexane. Next, the supernatant was separated into another centrifuge tube and again 4 ml of acetone was added, followed by centrifugation at 11,404g for 10 min. The pellet from this centrifugation will contain NPs of smaller size. These same steps of size centrifugation were continued till the supernatant became light pink in colour. All the NPs were further dispersed in acetone for future use.

Synthesis of PdAg NPs

The PdAg NPs were synthesized using a modified literature procedure by Sun et al.³². To a 50 ml RBF 0.2 mmol of AgNO₃, 0.2 mmol of PdCl₂ and 15 ml of OLA (70% O7805) were added and heated under vacuum to 110 °C and held for 30 min while stirring. Then the solution was heated to 210 °C under Ar and was maintained at this temperature for 60 min. Then, the solution was cooled until 70–80 °C followed by addition of 40 ml of IPA and 5 ml of hexane. Then the total solution was centrifuged at 2,050g for 10 min. After collecting the pellet, 3 ml of hexane and 20 ml of IPA were added. The solution was centrifuged for another 2,050g for 10 min. The pellet was dispersed in 3 ml of hexane and stored in acetone. In the case of polydisperse samples from NP fusion, size centrifugation similar to the AuCu NP synthesis was performed, with larger fused NPs precipitating out into the pellet before the non-fused NPs.

Synthesis of PdCo NPs

The PdCo NPs were made using a synthesis approach³³ from Sun et al. To a 100 ml RBF 0.3 mmol of Co(acac)₂, 0.2 mmol of PdBr₂ were mixed with 18 ml of OLA (70% O7805). The mixture was heated under a vacuum while stirring at 60 °C and kept for 20 min. Then 1 ml of TOP was added to the solution rapidly, and the mixture was heated to 260 °C under an inert Ar atmosphere for 1 h. Then, the solution was cooled till 70–80 °C and 25 ml of hexane added. The solution was added to a centrifuge tube and was centrifuged at 2,050g for 10 min to remove any large particles. The supernatant was separated, and 15 ml of acetone and 10 ml of ethanol added. Next, the solution was centrifuged for 11,404g for 10 min. The pellet was dispersed in 3 ml of hexane and stored in acetone.

Synthesis of Pd₃Sn NPs

The Pd₃Sn NPs were synthesized by a modified procedure previously described by the Skrabalak group³⁹. To synthesize Pd₃Sn NPs, PdBr₂ (0.16 mmol), Sn(ac)₂ (0.04 mmol), 9 ml of OLA (>70% 909831), 80 μl of TOP and 20 μl of OA were added to a 100 ml three-neck RBF, which was then heated under vacuum while stirring at 110 °C and held at temperature for 16 min. Then, the reaction solution was heated to 235 °C under Ar and held at that temperature for 20 min. Then, the solution was cooled to room temperature and centrifuged at 2,050g for 10 min with hexane to remove any large particles. The rest of the particles (contained in the collected supernatant) were precipitated by adding a

mixture of 3:1 acetone:ethanol, followed by collection by centrifugation at 11,404g. The NPs were stored in acetone for the next steps.

Synthesis of core–shell NPs

To synthesize core–shell NPs, bimetallic cores (0.02–0.06 mmol) were added to a 100 ml three-neck RBF containing 4 ml of OLA (70% O7805), 5 ml ODE, PtBr₂, Ni(acac)₂ and Pd(ac)₂. The concentrations of the metal precursors were calculated by considering a molar ratio of 1:1 of [seed/core] to [metal precursors]. 1,2-Dodecanediol was added with a 20:1 DDD: [seed/core] at the same time (for the core–shell AuCu@PtPdNi NPs, DDD was not needed in the synthesis). This reaction solution was first stirred at room temperature for 10 min and then heated to 110 °C under a vacuum and held at that temperature for 30 min. Then, the temperature was increased to 235 °C under an Ar blanket and was allowed to incubate for 30 min. The solution was allowed to cool down to 70–80 °C and 10 ml hexane was added. Then the solution was centrifuged at 2,050g for 10 min to remove any large particles. The rest of the particles (contained in the collected supernatant) were precipitated by adding a mixture of 3:1 acetone:ethanol, followed by collection by centrifugation at 11,404g. After the removal of the supernatant, the particles were finally resuspended in hexane for further use. Preparation of different core–shell NPs were obtained using the same method but with the metal precursors designated in the manuscript according to the shell compositional precursors.

Synthesis of HEA NPs

The obtained core–shell NPs were deposited on carbon support (Ketjen EC-300JD) by considering a mass ratio of 1:10. This ratio can be anywhere from 1:5 to 1:10 w/w core–shell seed:carbon to limit NP coalescences. The NPs were measured using a weighing balance after drying the solvent. After weighing, the dried NPs were re-dispersed in hexane (sometimes one drop of OLA was needed to fully disperse). Meanwhile required amount of carbon was taken in a 10 ml scintillating vial and sonicated with 5 ml acetone and 2.5 ml hexane. The NP solution then was added dropwise to the carbon slurry stirring with a stir bar. The addition speed was 10 µl per 5 s, and a syringe pump was used to add the core–shell NPs solution to the carbon slurry. Once the NPs were added, the solution was sonicated for 1 h and then left to stir overnight. The solvents were then evaporated with N₂ flow, and the resulting solids were dissolved in 1–2 ml of acetone by sonicating and transferred onto a quartz crucible. The boat was centred in a fused silica tube and heated in a tube furnace. The fused silica tube was purged with an H₂/N₂ (4 v/v%) mixture for 30 min, and then the samples were heated to 800 °C (600 °C, 500 °C, 400 °C and 300 °C for 30 min for the temperature-resolved study) for 2 h at a ramp rate of 35 °C min⁻¹. When supporting or dispersing core–shell NPs in titania, the same protocol was adhered to, with an equal weight of titania being used instead of ketjen carbon (1:10 w/w core@sell:titania).

Data availability

The data that substantiate the study's findings and contribute to the assessment of the paper's conclusions can be accessed within the paper and its Supplementary Information. Source data are provided with this paper.

References

- George, E. P., Raabe, D. & Ritchie, R. O. High-entropy alloys. *Nat. Rev. Mater.* **4**, 515–534 (2019).
- Zhou, M., Li, C. & Fang, J. Noble-metal based random alloy and intermetallic nanocrystals: syntheses and applications. *Chem. Rev.* **121**, 736–795 (2021).
- Yeh, J.-W. et al. Nanostructured high-entropy alloys with multiple principal elements: novel alloy design concepts and outcomes. *Adv. Eng. Mater.* **6**, 299–303 (2004).
- Cantor, B., Chang, I. T. H., Knight, P. & Vincent, A. J. B. Microstructural development in equiatomic multicomponent alloys. *Mater. Sci. Eng. A* **375–377**, 213–218 (2004).
- Wang, B. et al. General synthesis of high-entropy alloy and ceramic nanoparticles in nanoseconds. *Nat. Synth.* **1**, 138–146 (2022).
- Ding, Q. et al. Tuning element distribution, structure and properties by composition in high-entropy alloys. *Nature* **574**, 223–227 (2019).
- Banko, L. et al. Unravelling composition–activity–stability trends in high entropy alloy electrocatalysts by using a data-guided combinatorial synthesis strategy and computational modeling. *Adv. Energy Mater.* **12**, 2103312 (2022).
- Bueno, S. L. A. et al. Quinary, senary, and septenary high entropy alloy nanoparticle catalysts from core@shell nanoparticles and the significance of intraparticle heterogeneity. *ACS Nano* **16**, 18873–18885 (2022).
- Chen, Y. et al. Synthesis of monodisperse high entropy alloy nanocatalysts from core@shell nanoparticles. *Nanoscale Horiz.* **6**, 231–237 (2021).
- Feng, G. et al. Sub-2 nm ultrasmall high-entropy alloy nanoparticles for extremely superior electrocatalytic hydrogen evolution. *J. Am. Chem. Soc.* **143**, 17117–17127 (2021).
- Zhan, C. et al. Subnanometer high-entropy alloy nanowires enable remarkable hydrogen oxidation catalysis. *Nat. Commun.* **12**, 6261 (2021).
- Yao, Y. et al. Carbothermal shock synthesis of high-entropy-alloy nanoparticles. *Science* **359**, 1489–1494 (2018).
- Dey, G. R., McCormick, C. R., Soliman, S. S., Darling, A. J. & Schaak, R. E. Chemical insights into the formation of colloidal high entropy alloy nanoparticles. *ACS Nano* **17**, 5943–5955 (2023).
- Cao, G. et al. Liquid metal for high-entropy alloy nanoparticles synthesis. *Nature* **619**, 73–77 (2023).
- Li, H. et al. Fast site-to-site electron transfer of high-entropy alloy nanocatalyst driving redox electrocatalysis. *Nat. Commun.* **11**, 5437 (2020).
- Silva, C. M. D. et al. Colloidal synthesis of nanoparticles: from bimetallic to high entropy alloys. *Nanoscale* **14**, 9832–9841 (2022).
- Broge, N. L. N., Bertelsen, A. D., Søndergaard-Pedersen, F. & Iversen, B. B. Facile solvothermal synthesis of Pt–Ir–Pd–Rh–Ru–Cu–Ni–Co high-entropy alloy nanoparticles. *Chem. Mater.* **35**, 144–153 (2023).
- Ortiz, N. & Skrabalak, S. E. On the dual roles of ligands in the synthesis of colloidal metal nanostructures. *Langmuir* **30**, 6649–6659 (2014).
- Gilroy, K. D., Ruditskiy, A., Peng, H.-C., Qin, D. & Xia, Y. Bimetallic nanocrystals: syntheses, properties, and applications. *Chem. Rev.* **116**, 10414–10472 (2016).
- Louidice, A. & Buonsanti, R. Reaction intermediates in the synthesis of colloidal nanocrystals. *Nat. Synth.* **1**, 344–351 (2022).
- De Roo, J. Chemical considerations for colloidal nanocrystal synthesis. *Chem. Mater.* **34**, 5766–5779 (2022).
- Muzzio, M. et al. Monodisperse nanoparticles for catalysis and nanomedicine. *Nanoscale* **11**, 18946–18967 (2019).
- McCormick, C. R., Katzbaer, R. R., Steimle, B. C. & Schaak, R. E. Combinatorial cation exchange for the discovery and rational synthesis of heterostructured nanorods. *Nat. Synth.* **2**, 152–161 (2023).
- Vasquez, Y., Henkes, A. E., Chris Bauer, J. & Schaak, R. E. Nanocrystal conversion chemistry: a unified and materials-general strategy for the template-based synthesis of nanocrystalline solids. *J. Solid State Chem.* **181**, 1509–1523 (2008).

25. Xia, X., Wang, Y., Ruditskiy, A. & Xia, Y. 25th anniversary article: galvanic replacement: a simple and versatile route to hollow nanostructures with tunable and well-controlled properties. *Adv. Mater.* **25**, 6313–6333 (2013).
26. Gamler, J. T. L. et al. Achieving highly durable random alloy nanocatalysts through intermetallic cores. *ACS Nano* **13**, 4008–4017 (2019).
27. DeSantis, C. J., Sue, A. C., Bower, M. M. & Skrabalak, S. E. Seed-mediated co-reduction: a versatile route to architecturally controlled bimetallic nanostructures. *ACS Nano* **6**, 2617–2628 (2012).
28. Lide, D. R. *CRC Handbook of Chemistry and Physics, 89th ed.* (CRC Press, Taylor & Francis: Boca Raton, FL, 2008).
29. Kar, N. et al. Reaction stoichiometry directs the architecture of trimetallic nanostructures produced via galvanic replacement. *Nanoscale* **15**, 3749–3756 (2023).
30. Ashberry, H. M., Gamler, J. T. L., Unocic, R. R. & Skrabalak, S. E. Disorder-to-order transition mediated by size refocusing: a route toward monodisperse intermetallic nanoparticles. *Nano Lett.* **19**, 6418–6423 (2019).
31. Vegard, L. & Dale, H. VIII. Untersuchungen über Mischkristalle und Legierungen. *Z. Krist. Cryst. Mater* **67**, 148–162 (1928).
32. Sun, D. et al. Monodisperse AgPd alloy nanoparticles as a highly active catalyst towards the methanolysis of ammonia borane for hydrogen generation. *RSC Adv.* **6**, 105940–105947 (2016).
33. Sun, D., Mazumder, V., Metin, Ö. & Sun, S. Catalytic hydrolysis of ammonia borane via cobalt palladium nanoparticles. *ACS Nano* **5**, 6458–6464 (2011).
34. mp-1022725: Sn (Cubic, Fm-3m, 225). *The Materials Project* https://materialsproject.org/materials/mp-1022725?chemsys=Sn#literature_references (2023)
35. Almeida, T. S., Van Wassen, A. R., VanDover, R. B., de Andrade, A. R. & Abruña, H. D. Combinatorial PtSnM (M = Fe, Ni, Ru and Pd) nanoparticle catalyst library toward ethanol electrooxidation. *J. Power Sources* **284**, 623–630 (2015).
36. Rizo, R. et al. Pt-Richcore/Sn-Richsurface/Ptskin nanocubes as highly active and stable electrocatalysts for the ethanol oxidation reaction. *J. Am. Chem. Soc.* **140**, 3791–3797 (2018).
37. Zhao, X., Yang, Q. & Quan, Z. Tin-based nanomaterials: colloidal synthesis and battery applications. *Chem. Commun.* **55**, 8683–8694 (2019).
38. Kravchyk, K. et al. Monodisperse and inorganically capped Sn and Sn/SnO₂ nanocrystals for high-performance Li-ion battery anodes. *J. Am. Chem. Soc.* **135**, 4199–4202 (2013).
39. Bueno, S. L. A., Zhan, X., Wolfe, J., Chatterjee, K. & Skrabalak, S. E. Phase-controlled synthesis of Pd–Sn nanocrystal catalysts of defined size and shape. *ACS Appl. Mater. Interfaces* **13**, 51876–51885 (2021).
40. Ashberry, H. M., Zhan, X. & Skrabalak, S. E. Identification of nanoscale processes associated with the disorder-to-order transformation of carbon-supported alloy nanoparticles. *ACS Mater. Au* **2**, 143–153 (2022).
41. Gao, S. et al. Synthesis of high-entropy alloy nanoparticles on supports by the fast moving bed pyrolysis. *Nat. Commun.* **11**, 2016 (2020).
42. Hansen, P. L. et al. Atom-resolved imaging of dynamic shape changes in supported copper nanocrystals. *Science* **295**, 2053–2055 (2002).
43. Xie, C., Niu, Z., Kim, D., Li, M. & Yang, P. Surface and interface control in nanoparticle catalysis. *Chem. Rev.* **120**, 1184–1249 (2020).
44. Harak, E. W., Koczur, K. M., Harak, D. W., Patton, P. & Skrabalak, S. E. Designing efficient catalysts through bimetallic architecture: Rh@Pt nanocubes as a case study. *ChemNanoMat* **3**, 815–821 (2017).

Acknowledgements

S.E.S., N.K., M.M., I.H.S., J.W. and S.L.A.B. acknowledge financial support from Indiana University and the US National Science Foundation (NSF CHE 2203349 received by S.E.S.). The authors acknowledge support from Indiana University's Electron Microscopy Center, XPS facility (access to XPS at the Nanoscale Characterization Facility was provided by the NSF Award DMR MRI-1126394 received by S.E.S.), and Nanoscale Characterization Facility for access to instrumentation. They also thank X. Zhan, E. Verma and Y. Losovyj for their helpful discussions.

Author contributions

N.K. and S.E.S. were responsible for the project concept and design of experiments. N.K. developed the synthesis of bimetallic and core-shell NPs and characterizations. M.M. and J.W. helped in synthesis of AuCu and Pd₃Sn core-shell NP synthesis, respectively. I.H.S. contributed in temperature-dependent experiments. S.L.A.B. contributed some STEM-EDS characterization as well as some control experiments. This manuscript was written through the contributions of all authors. All authors have given approval to the final version of this manuscript.

Competing interests

The authors declare no competing financial interest.

Additional information

Supplementary information The online version contains supplementary material available at <https://doi.org/10.1038/s44160-023-00409-0>.

Correspondence and requests for materials should be addressed to Sara E. Skrabalak.

Peer review information *Nature Synthesis* thanks Zhiming Li and the other, anonymous, reviewer(s) for their contribution to the peer review of this work. Alexandra Groves, in collaboration with the *Nature Synthesis* team.

Reprints and permissions information is available at www.nature.com/reprints.

Publisher's note Springer Nature remains neutral with regard to jurisdictional claims in published maps and institutional affiliations.

Springer Nature or its licensor (e.g. a society or other partner) holds exclusive rights to this article under a publishing agreement with the author(s) or other rightsholder(s); author self-archiving of the accepted manuscript version of this article is solely governed by the terms of such publishing agreement and applicable law.

© The Author(s), under exclusive licence to Springer Nature Limited 2023